BAMS Article

Going to Extremes

Installing the World's Highest Weather Stations on Mount Everest

T. Matthews, L. B. Perry, I. Koch, D. Aryal, A. Khadka, D. Shrestha, K. Abernathy, A. C. Elmore, A. Seimon, A. Tait, S. Elvin, S. Tuladhar, S. K. Baidya, M. Potocki, S. D. Birkel, S. Kang, T. C. Sherpa, A. Gajurel, and P. A. Mayewski

ABSTRACT: As the highest mountain on Earth, Mount Everest is an iconic peak that offers an unrivalled natural platform for measuring ongoing climate change across the full elevation range of Asia's water towers. However, Everest's extreme environment challenges data collection, particularly on the mountain's upper slopes, where glaciers accumulate mass and mountaineers are most exposed. Weather stations have operated on Everest before, including the world's previous highest, but coverage has been sparse in space and time. Here we describe the installation of a network of five automatic weather stations (AWSs), including the two highest stations on Earth (8,430 and 7,945 m MSL) which greatly improves monitoring of this iconic mountain. We highlight sample applications of the new data, including an initial assessment of surface energy fluxes at Camp II (6,464 m MSL) and the South Col (7,945 m MSL), which suggest melt occurs at both sites, despite persistently below-freezing air temperatures. This analysis indicates that melt may even be possible at the 8,850 m MSL summit, and prompts a reevaluation of empirical temperature index models used to simulate glacier melt in the Himalayas that focus only on air temperature. We also provide the first evaluation of numerical weather forecasts at almost 8,000 m MSL and use of model output statistics to reduce forecast error, showcasing an important opportunity to improve climber safety on Everest. Looking forward, we emphasize the considerable potential of these freely available data for understanding weather and climate in the Himalayas and beyond, including tracking the behavior of upper-atmosphere winds, which the AWS network is uniquely positioned to monitor.

https://doi.org/10.1175/BAMS-D-19-0198.1
Corresponding author: T. Matthews, t.matthews@lboro.ac.uk
In final form 17 May 2020

AFFILIATIONS: Matthews—Department of Geography and Environment, Loughborough University, Loughborough, United Kingdom; **Perry and Seimon**—Department of Geography and Planning, Appalachian State University, Boone, North Carolina; **Koch and Sherpa**—International Centre for Integrated Mountain Development, Lalitpur, Nepal; **Aryal and Shrestha**—Central Department of Hydrology and Meteorology, Tribhuvan University, Kathmandu, Nepal; **Khadka**—International Centre for Integrated Mountain Development, Lalitpur, and Central Department of Hydrology and Meteorology, Tribhuvan University, Kathmandu, Nepal; **Abernathy, Elmore, Tait, and Elvin**—National Geographic Society, Washington, D.C.; **Tuladhar and Baidya**—Department of Hydrology and Meteorology, Kathmandu, Nepal; **Potocki**—Climate Change Institute, University of Maine, Orono, Maine and School of Earth and Climate Sciences, University of Maine, Orono, Maine; **Birkel and Mayewski**—Climate Change Institute, University of Maine, Orono, Maine; **Kang**—State Key Laboratory of Cryospheric Science, Northwest Institute of Eco-Environment and Resources, Chinese Academy of Sciences, Lanzhou, and Center for Excellence in Tibetan Plateau Earth Sciences, Chinese Academy of Sciences, Beijing, China; **Gajurel**—Central Department of Geology, Tribhuvan University, Kathmandu, Nepal

Mountains cover 25% of Earth's land surface and their snow and ice stores act as water towers for more than a billion people worldwide (Immerzeel et al. 2020, 2010; Meybeck et al. 2001; Viviroli et al. 2007). They are locations of especially hazardous weather extremes (Moore and Semple 2006; Wang et al. 2015), and a natural observation platform from which to observe globally significant high-altitude winds (Abish et al. 2015; Moore and Semple 2004). The climate is also warming at altitude more rapidly than the global mean, which makes these water towers vulnerable to accelerated melt (Mountain Research Initiative EDW Working Group 2015). It is unfortunate, then, that continuous observations from automatic weather stations (AWSs) are biased toward lower, more accessible elevations (Fig. 1). The problem is particularly apparent in High Mountain Asia (HMA), where only a handful of AWSs have been installed above 5,000 m MSL, an elevation above which almost 62,000 km^2 of glacier area in HMA is located (around 63% of the total HMA glacierized area); above 6,000 m MSL nearly 11,000 km^2 (around 11% of the glacierized area) is found, yet we were unaware of a single AWS in HMA still operating above this elevation when our project started (observations from 6,352 m MSL on Nepal's Mera Peak ceased in November 2016).

Perhaps the most ambitious prior effort to fill the high-altitude observational gap was by the Everest–K2–National Research Council (Ev-K2-CNR) Committee (Locci et al. 2014) which, beginning in 1993, established a network of six AWSs from 2,660 to almost 8,000 m MSL on the Nepalese side of Everest (also known in local languages as Sagarmatha or Qomolangma), and included the world's highest AWS at Everest's South Col (Bertolani et al. 2000; Salerno et al. 2015). That network has provided valuable insights, including the assessment of dangerous weather events high on Everest (Moore and Semple 2011), and the identification of emerging climate trends (Salerno et al. 2015). It has also been used to help drive glacier mass balance models (Shea et al. 2015). However, the quality and number of observations from the AWSs is reduced at higher elevations, with the South Col record particularly short and fragmentary. The Ev-K2-CNR installation there was performed by a team of Italians and Nepalis in May 2008 (Moore et al. 2012), building on previous, very short-term deployments by North American researchers in both 1996 (Lau 1998) and 1998 (Moore and Semple 2004). Air temperature data were available intermittently from the Ev-K2-CNR South Col station until 2011, when the AWS was apparently destroyed by wind-blown debris, highlighting the extremely challenging environment for prolonged data collection (G. P. Verz 2019, personal communication). Since 2011, the highest AWSs installed in the Khumbu region were on Kala Patthar summit and Changri Nup Glacier, at altitudes of 5,600 and 5,700 m MSL, respectively

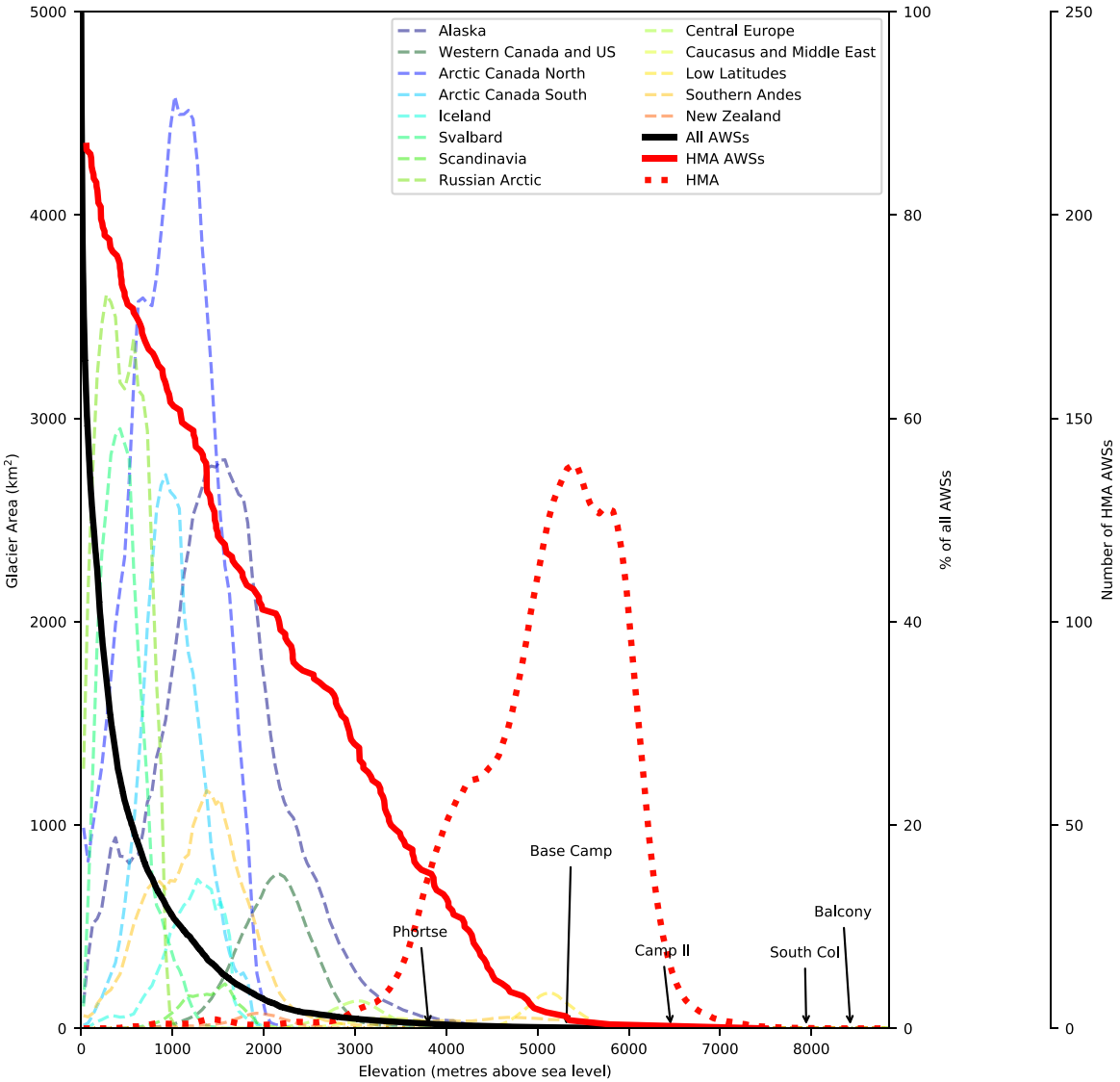

Fig. 1. Percentage of all active AWSs above the elevation marked on the *x* axis, and the number of AWSs in High Mountain Asia (HMA) above the respective elevation, as identified from the Integrated Surface Database (Smith et al. 2011), with AWSs added from additional high-altitude networks known to the authors (see appendix A). The elevations of the new AWSs from the 2019 Everest Expedition discussed in the text are annotated with arrows. Dotted and dashed lines give the glacier area–altitude distribution (hypsometry) for all glacier regions in the Randolph Glacier inventory (Pfeffer et al. 2014), excluding Antarctica and Greenland. Note that the HMA curve is the sum of glacier areas in the Central Asia, South Asia West, and South Asia East regions.

(Locci et al. 2014; Salerno et al. 2015). On the Chinese (north) side of Everest, AWSs have been deployed at the North Col (7,028 m MSL) and the Ruopula Pass (6,560 m MSL) (Yang et al. 2011), but they have not been active since 2008 and 2010, respectively.

There are very strong scientific and human safety motivations to establish a new network of AWSs high on Everest. First, around 20% of the surface area, and almost all of the accumulation zones of the glaciers in the Dudh Koshi River basin (within which the Khumbu region is located) are situated above 5,800 m MSL (Salerno et al. 2015; Shea et al. 2015), meaning there is currently no in situ monitoring of climate variables at elevations critical for regional water-resource monitoring. Second, the extreme altitude enables direct and continuous monitoring of the jet stream winds—globally significant circulation features that may be changing in strength and location as the climate warms (Abish et al. 2015). Third, climbers continue to attempt to summit Everest in growing numbers, and deterioration in the weather

is a major contributor to death rates high on the mountain (Firth et al. 2008), where weather observations are absent and the performance of forecasts unknown.

Considering these motivations, we undertook an ambitious program to install a network of five AWSs during the premonsoon climbing season of 2019 as part of the National Geographic and Rolex Perpetual Planet Expedition to Mount Everest (hereafter 2019 Everest Expedition). This effort was spearheaded by the meteorology team on what was an ambitious multidisciplinary expedition that also included glaciology, biology, geology, and mapping components (National Geographic 2019). In what follows, we describe the installation of this network, including the design specification of the stations for the extreme environment. We then show preliminary data collected by the network and highlight their utility in addressing some of the motivations explained above. We close by highlighting potential avenues for future research utilizing this new, freely available data source.

Network design

Site selection. To improve weather monitoring in the Khumbu region, the 2019 Everest Expedition planned not only to extend the measurement network to new heights, but also to improve the density and quality of observations at lower elevations. At present, a lack of basic hydrometeorological observations in the region inhibits understanding of evolving water resources under climate change (Krishnan et al. 2019; You et al. 2017). We aimed to help fill this gap by installing AWSs that monitor liquid and solid precipitation and snow depth and variables required to resolve the surface energy fluxes (Wild et al. 2017; Table 1).

Five potential sites for AWS deployments were selected based on the following: 1) the anticipated utility of measurements from each location, and 2) the logistical challenges of installation and longer-term maintenance (Fig. 2). The lowest of these sites, Phortse (3,810 m), was selected because its abundant flat ground and largely unobstructed sky provides an

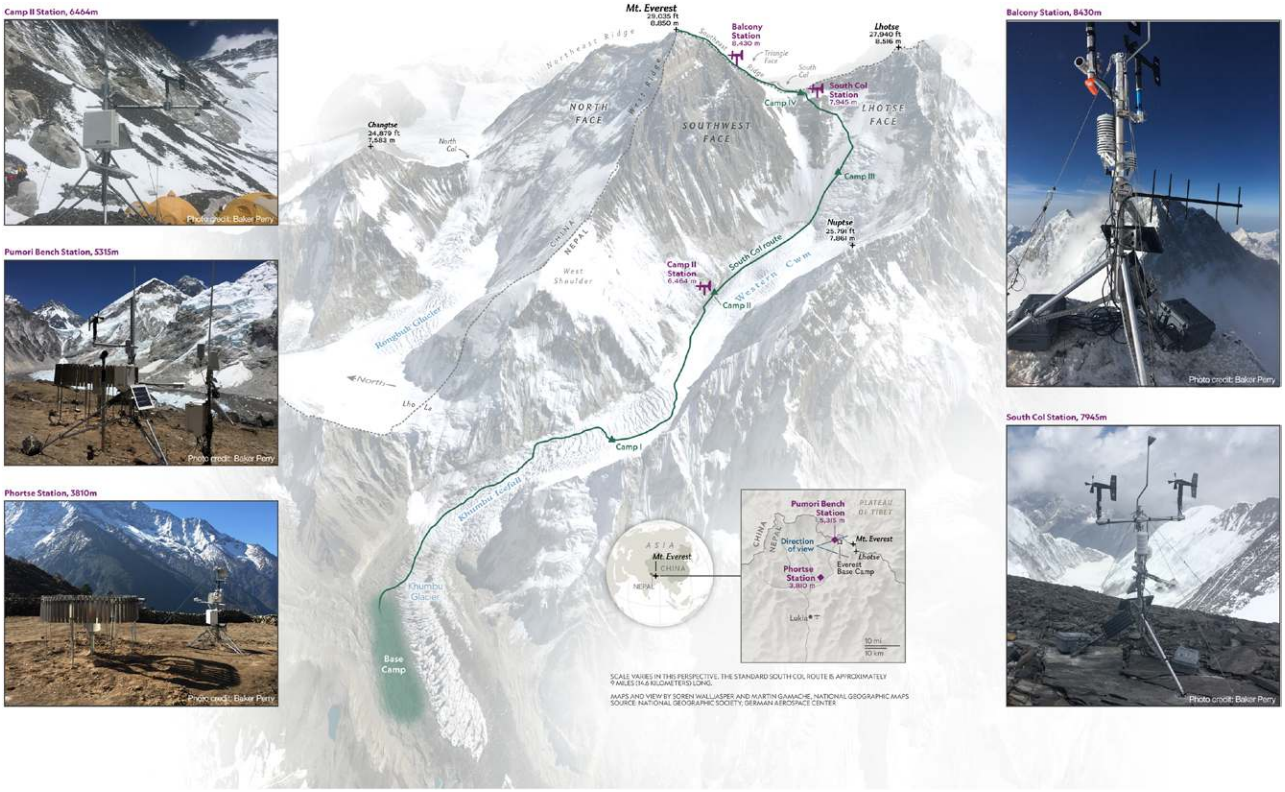

Fig. 2. (center) Map of locations referred to in the text. (left),(right) Photographs of the automatic weather stations installed during the 2019 Everest Expedition. (top right) Note the shovel handles used to mount the wind speed sensors on the Balcony weather station.

Table 1. AWS specifications for each of the five sites. Note that weights are only provided for the highest stations, which needed to be hand carried to their install sites.

	Phortse	Base Camp	Camp II	South Col	Balcony
Latitude (°N)	27.8456	27.9952	27.9810	27.9719	27.9826
Longitude (°E)	86.7472	86.8406	86.9023	86.9295	86.9292
Elevation (m MSL)	3,810	5,315	6,464	7,945	8,430
Operation	24 Apr 2019–present	10 Oct 2019–present	9 Jun 2019–present	22 May 2019–present	23 May 2019–present
Above-ground sensor level (m)	2 m for temperature and humidity, 2.3 m for wind	2 m	2 m	1.5 m for temperature and humidity, 2 m for wind	1.5 m for temperature and humidity, 2 m for wind
Air temperature sensor	Vaisala HMP155A-L5-PT; CS109	Vaisala HMP155A-L5-PT; CS109	Vaisala HMP155A-L5-PT; CS109	Vaisala HMP155A-L5-PT; CS109	Vaisala HMP155A-L5-PT; CS109
Relative humidity sensor	Vaisala HMP155A-L5-PT	Vaisala HMP155A-L5-PT	Vaisala HMP155A-L5-PT	Vaisala HMP155A-L5-PT	Vaisala HMP155A-L5-PT
Wind speed and direction sensor	R. M. Young 05108-45	R. M. Young 05108-45	R. M. Young 05108-45	2 × R. M. Young 05108-45	2 × R. M. Young 05108-45
Air pressure sensor	Vaisala PTB 110	Vaisala PTB210	Vaisala PTB210	Vaisala PTB210	Vaisala PTB210
Radiation sensor	2 × Hukseflux SR30 (up/down shortwave radiation); 2 × Hukseflux IR20 (up/down thermal radiation)	Hukseflux NR01	Apogee SN-500-SS	Hukseflux NR01	—
Precipitation sensor	OTT Pluvio 2 and double alter shield	OTT Pluvio 2 and double alter shield	—	—	—
Present-weather sensor	OTT Parsivel 2	OTT Parsivel 2	—	—	—
Relative surface elevation change sensor	Campbell Scientific SR50A	Campbell Scientific SR50A	Campbell Scientific SR50A	—	—
Datalogger	Campbell Scientific CR1000X	Campbell Scientific CR1000X	Campbell Scientific CR1000X	Campbell Scientific CR1000X	Campbell Scientific CR1000X
Logger enclosure	Standard	Standard	Standard	Pelican case with military-spec quick connects	Pelican case with military-spec quick connects
Batteries	24 Ah	3 × 8 Ah	3 × 8Ah	3 × 8 Ah	3 × 8 Ah
Charging	2 × 20-W solar panels	2 × 20-W solar panels	2 × 20-W solar panels	2 × 10-W solar panels	2 × 10-W solar panels
Telemetry	Inmarsat	Thuraya; 400-MHz radio	Thuraya	Thuraya; 400-MHz radio	Thuraya; 400-MHz radio
Sampling interval	3 s (wind); 60 s (radiation, air pressure, temperature, relative humidity, precipitation); 3,600 s (present weather, relative surface elevation change)	5 s (wind); 60 s (temperature, relative humidity, precipitation); 600 s (air pressure); 3,600 s (present weather)	60 s (temperature, relative humidity, wind); 600 s (radiation); 3,600 s (relative surface elevation change)	5 s (wind); 60 s (temperature, relative humidity, radiation); 600 s (pressure)	5 s (wind); 60 s (temperature, relative humidity); 600 s (pressure)
Tripod	Campbell Scientific CM106B	Campbell Scientific CM106B	Campbell Scientific CM106B	Custom Aluminum	Custom Aluminum
Approximate weight	Not available	Not available	Not available	Total: 50 kg Pelican case with logger: 8 kg Pelican case with batteries: 16 kg Tripod: 7 kg Crossarms, mounts, and bolts: 11 kg Sensors: 8 kg	Total: 50 kg Pelican case with logger: 8 kg Pelican case with batteries: 16 kg Tripod: 7 kg Crossarms, mounts, and bolts: 11 kg Sensors: 8 kg

excellent location for measuring radiation and precipitation (including a double-alter wind shield). The Pumori Bench (5,315 m), a vegetated medial moraine close to Everest's Base Camp, was chosen as the only other location below the Khumbu Ice Fall (a dangerous obstacle to climbers). This site enables weather observations representative of the Khumbu Glacier's upper, clean-ice ablation area (Rounce et al. 2018), an area of interest to glacier–climate studies (Pratap et al. 2015). The Pumori Bench is also relatively stable, and therefore suitable for precipitation sensors and a double-alter wind shield. Due to its proximity to such a well-known location on the Everest climbing route, we refer to this station as "Base Camp" hereafter.

Above the Khumbu Ice Fall, we selected sites at Everest's Camp II (~6,400 m MSL), the South Col (~7,900 m MSL), and as close to Everest's 8,850 m MSL summit as possible. All these locations are along the main southern Nepalese Everest climbing route, which maximizes accessibility for maintenance visits. Camp II represents the approximate maximum elevation of the 0°C isotherm in the Khumbu region according to Shea et al. (2015), and is therefore an opportune site for tracking this important meteoric parameter for glacier mass balance (Bradley et al. 2009; Carrasco et al. 2005). In the interests of data continuity, we aimed to install the new South Col AWS on bedrock close to the previous Italian station. For the uppermost station, a number of possible sites were identified in appreciation of the challenges posed by journeying to 8,850 m MSL, including the "Balcony" (8,430 m MSL) and South Summit (8,749 m MSL).

Design specification. A critical part of preparing the network was identifying the likely demands on the highest AWSs from extreme weather. To guide us, we used ERA-Interim data from the European Centre for Medium-Range Weather Forecasts (ECMWF; Dee et al. 2011), interpolating 6-hourly wind speeds and air temperatures from the closest model levels to the latitude, longitude, and elevation of the summit. These prefieldwork results indicated a maximum wind speed of 76 m s^{-1}, and a minimum temperature of −49°C during 1979–2018 (Fig. 3). However, the former refers to means rather than instantaneous gusts, so we multiplied by 1.4 (a representative gust factor for strong winds in mountainous terrain; Ágústsson and Ólafsson 2004) to obtain a precautionary estimate of extreme winds. This scaling updated the maximum wind speed to around 106 m s^{-1} which, if reached, would surpass the world record outside a tropical cyclone or tornado (WMO 2019). We took this as our design standard for wind speed (for both the South Col and summit), and also ensured that the AWSs should be resilient to temperatures of −60°C and an atmospheric pressure of 311 hPa (the minimum value in the reanalysis data for the summit).

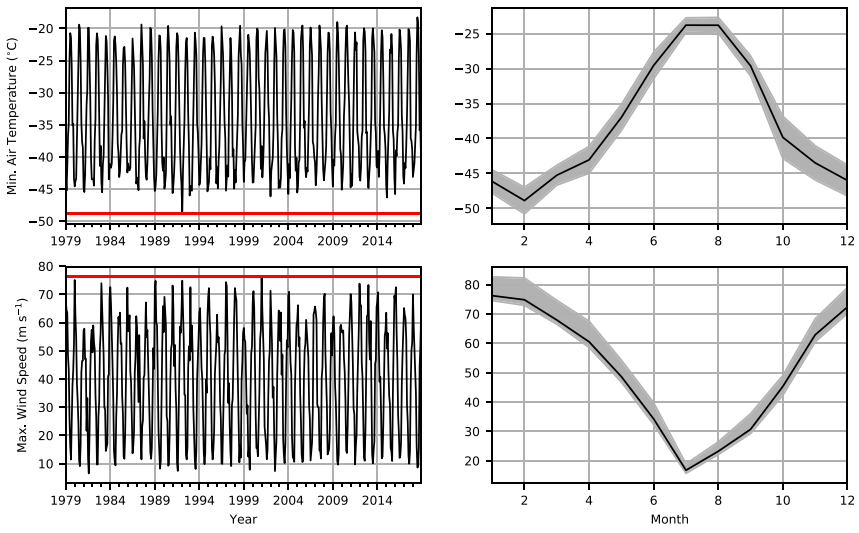

Fig. 3. Extreme (left) temperatures and (right) wind speeds in the ERA-Interim data at the summit of Everest (8,850 m MSL), 1979–2018. (top left) Monthly time series of minimum temperature, with red line highlighting the all-time minimum (−49°C). (bottom left) Monthly time series of maximum wind speed (all-time maximum is 76 m s^{-1}). (top right) All-time minimum air temperature (line) in the reanalysis for the summit plus and minus one standard deviation of minima in that month across years. (bottom right) As in the top-right panel, but for maximum wind speeds.

The AWSs were designed with Campbell Scientific, Inc. (from which the stations were purchased) to cope with these extreme meteorological demands through a two-pronged approach. First, some sensors for

the two highest stations underwent special low-temperature modifications, and battery-heaters and insulation were added to safeguard the power supply. Telemetry and datalogging programs were also designed to be robust and conserve power, with double-redundant transmission (Thuraya satellite modem or radio transmission to Base Camp AWS), and a high-capacity micro-SD card in case transmission was paused due to low power. The second means of ensuring resilience of the two highest AWSs was to guard against the additional challenges of high wind and extreme low pressure. We did this by designing the custom tripods to be guy-wired and bolted to bedrock and planned for redundant temperature and wind speed sensors. We also subjected AWS sensors to a full system test in a low-temperature hypobaric chamber before deployment.

In addition to being robust, the summit and South Col AWSs had to be 1) lightweight, since they would be hand carried to extreme elevations; and 2) require minimal setup time (~1.5 h) due to the extreme environmental conditions facing the climbing team (e.g., limited supplementary oxygen, cold, fatigue). The total weight of each station was therefore limited to ~50 kg (Table 1). To facilitate a quick installation while wearing gloves/mittens, the tripod, cross arms, and all mounts were designed with twist knobs and/or pins with quick release handles. All sensor cables were also prewired to a Campbell Scientific CR1000x datalogger inside an insulated Pelican case with military-specification quick-connect fittings (Fig. 2).

Installation of the weather stations. Our team installed the AWS network in April and May 2019. The Phortse, Base Camp, and Camp II deployments used conventional tripods and were relatively straightforward; however, the two highest installations were considerably more complex given the extreme environmental conditions and logistics of carrying two 50-kg AWSs up the ~1,500-m-high Lhotse Face (Fig. 2). After a regimented acclimatization schedule and many training deployments of these custom AWSs, the team left Everest Base Camp on 18 May 2019 to install the uppermost stations, climbing to the South Col over four days. We installed the new AWS there approximately 30 m higher than the most recent Ev-K2-CNR deployment (Salerno et al. 2015), in an area farther from debris which could impact the station during periods of extreme winds. The first observation from the South Col AWS was received at 1145 Nepal time (NPT) 22 May 2019 indicating a temperature of –17.8°C, 53% relative humidity, 380-hPa pressure, and winds out of the west-southwest at 8.5 m s^{-1} gusting to 15 m s^{-1}, resulting in a wind chill of –29.8°C

The summit push began at 2300 NPT 22 May 2019. Our team of 22, including 14 Sherpas, 3 scientists (Matthews, Perry, Potocki), 3 media team members, and 2 Nepalese climbers, made substantial progress for the first 3 h. A traffic jam of climbers then slowed progress, consistent with the very narrow time window suitable for summitting according to available weather forecasts (Wilkinson 2019). Given the exceptionally slow pace and visible crowding farther up the route, safety concerns prompted us to install our highest AWS at the Balcony (the lowest targeted "summit" site), at around 0400 NPT.

The Balcony deployment was hindered by the extreme cold, with drill batteries (required to set the rock anchors for the tripod) needing to be warmed by body heat to restore their function. We also observed that the critical mounts for the wind sensors were missing, so improvised replacements using lightweight aluminum shovel handles approximately the same diameter as the original pipe mounts (Fig. 2). The installation of the world's first AWS above 8,000 m MSL was completed shortly before 0645 NPT 23 May 2019, with initial measurements of –23.9°C air temperature, 78% relative humidity, 355-hPa pressure, and winds out of the northeast at 1.7 m s^{-1} gusting to 5.5 m s^{-1}, translating to a wind chill of –29.6°C.

Initial observations. All except the Base Camp AWS[1] have been operating since the 2019 Everest Expedition and we focus here on interesting aspects of the record up to 31 October 2019. The

[1] The Base Camp station was offline from late May until mid-October due to a software bug (now corrected).

preliminary data (Fig. 4) highlight the considerable range of conditions spanned by the network in space and time, with the Balcony site on average 28°C lower in air temperature than the Phortse site (4,620 m below). Consistent with previous research we observe the temperature lapse rate to exhibit strong seasonality, including a shift to shallower values during the monsoon (Immerzeel et al. 2014; Kattel et al. 2013), which started around 1 July 2019. The decline in high altitude winds, increase in relative humidity, and initiation of substantial precipitation accumulations at Phortse, identify this monsoon onset and indicate a somewhat delayed arrival, with initiation normally earlier in June (Gautam and Regmi 2013; Immerzeel et al. 2014; Salerno et al. 2015). A relative drying of the atmosphere at all sites and acceleration of the high-altitude winds suggest termination around 1 October 2019, which is more consistent with the climatological timing of cessation (Gautam and Regmi, 2013). The apparent brevity of the monsoon is reflected in precipitation receipts, with 558 mm recorded at Phortse since installation (17 April to 31 October 2019) equivalent to around 90% of the climatological monsoonal precipitation for this altitude in the Koshi River basin (Salerno et al. 2015).[2]

The delayed monsoon onset is recognizable in comparisons of our observations at the South Col with those from the world's previous highest AWS operating there in 2008 (Moore et al. 2012), as our median June temperature was around 1.3°C lower, and the median wind speed was almost 3 m s^{-1} higher (Table 2). During July and August, the temperatures and wind speeds between years are in relatively close agreement, but Moore et al. (2012) report much stronger winds and lower air temperatures throughout September and October. Despite such apparently subdued winds during the postmonsoon period, our peak gust of 50.8 m s^{-1} exceeds the all-time maximum wind speed by a factor of 1.12 for October estimated from the ERA-Interim for the summit/South Col (45.3 m s^{-1}; "Design specification" section), a feat also achieved by June's 39.8 m s^{-1} gust (1.16 times greater than the 34.3 m s^{-1} maximum for that month in the ERA-Interim). These gust factors are well within the AWS design standard, but suggest that the all-time maximum values plotted in Fig. 4 are a lower bound for the winds to anticipate at the South Col. The Balcony AWS was evidently installed in a more sheltered location than the Col, with generally

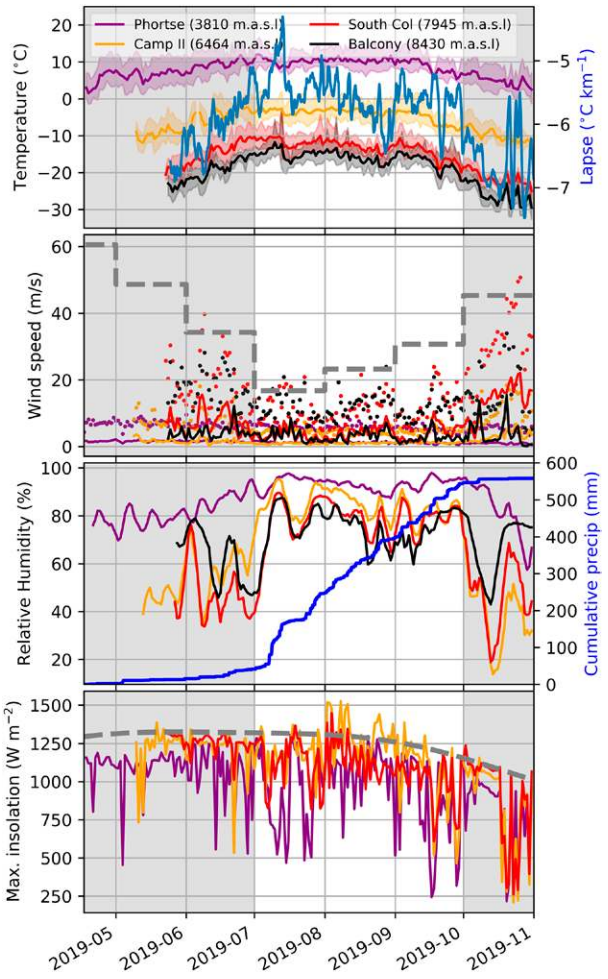

Fig. 4. Initial observations of selected variables at the AWSs. (top) Temperatures and lapse rates across all stations. Lapse rates were calculated as the slope coefficient from regressing running 24-h mean air temperature at the AWSs against their elevations. (top middle) Daily mean wind speeds (lines) and maximum gusts (points). The gray dotted line gives the all-time maximum wind speed in the ERA-Interim for the respective month. (bottom middle) Mean daily relative humidity smoothed with a 3-day running mean. Cumulative precipitation at Phortse is plotted on the right *y* axis. (bottom) Daily maximum insolation at the AWSs (note that the Balcony site does not have a pyranometer). The gray dashed line here is the top-of-atmosphere incident flux, calculated using a solar constant of 1,366 W m^{-2} and corrected for seasonal variations in Earth–sun distance. For all panels, the gray-shading highlights the nonmonsoonal period.

[2] Salerno et al. (2015) indicate mean annual precipitation (p) in the Koshi River basin can be modeled as a function of elevation x, according to $p = 21{,}168e^{-0.0009x}$, and that around 90% of this falls during the monsoon.

lower winds despite the greater elevation (Fig. 4). Note that the slightly reduced air pressure we recorded relative to 2008 in all months (Table 2) is consistent with the marginally higher elevation of our AWS compared with the Italian installation site.

Another interesting feature of the early observations is the extraordinary receipts of insolation at Phortse, Camp II, and the South Col, where daily maximum values approach, and occasionally exceed, the top-of-atmosphere incident flux (Fig. 4). Transmittance of solar radiation increases with elevation (Bintanja, 1996), but some attenuation of insolation from ozone, water vapor, and uniformly mixed gases should be anticipated (Pellicciotti et al. 2011). Insolation exceeding the top-of-atmosphere potential has been reported before in the Himalaya, and is thought to result from multiple reflections from nearby snow-covered surfaces and thin clouds (de Kok et al. 2020). We suggest that further analysis of this phenomenon should be considered, given the potential importance of shortwave radiation in driving high-altitude melt and sublimation identified below.

Table 2. Comparison between monthly medians at the South Col from the new AWS (left columns of each variable, 2019 values) and those from the world's previous highest AWS at the South Col (right column of each variable, 2008 values) (Moore et al. 2012b).

	Air pressure (hPa)		Air temperature (°C)		Wind speed (m s^{-1})	
Month	2019	2008	2019	2008	2019	2008
Jun	382.5	385.2	–14.2	–12.9	6.9	3.9
Jul	383.7	386	–11.7	–11.9	2.9	2.8
Aug	384.5	386.2	–13	–12.6	4.3	2.4
Sep	384.2	385.4	–14.7	–16.4	3.2	9.4
Oct	379.8	380.7	–21.7	–23	14.4	20

Sample applications

Glacier–climate interactions. The South Col and Camp II AWSs are instrumented to model the surface energy fluxes at elevations rarely possible, offering the opportunity to improve regional simulations of glacier mass balance in HMA. We explore the energetics at these locations using a model (detailed in appendix B) that computes all terms in the surface energy balance (SEB):

$$0 = Q_{\mathrm{SW}} + Q_{\mathrm{LW}} + Q_H + Q_L + Q_G + Q_M, \tag{1}$$

where Q_{SW} is the net shortwave heat flux, Q_{LW} is the net longwave heat flux, Q_H is the sensible heat flux, Q_L is the latent heat flux, Q_G is the ground heat flux, and Q_M is the energy available for melting. The SEB was modeled for a prescribed snow surface with constant albedo (0.8); because the AWSs are located on bedrock proximate to the glacier (Fig. 2), so we are unable to monitor the evolving glacier surface directly.

Consistent with previous studies in the region (Kayastha et al. 1999; Litt et al. 2019), and following from the high levels of insolation reported in the initial observations, the results indicate that net shortwave radiation is the largest energy source for the surface at both sites (Fig. 5 and Table 3). Most of this energy is then dissipated by net longwave radiation, with smaller amounts lost to the latent heat flux (sublimation) and consumed in melting. The SEB modelling indeed indicates that the amount of potential meltwater generated at Camp II is non-negligible, despite freezing air temperatures (Figure 5; 77% of melt occurred when air temperature was below 0°C). This conclusion was supported by streams of meltwater observed in the vicinity of Camp II during May on the 2019 Everest Expedition, a month in which air temperature did not rise above freezing for a single hour at the Camp II AWS. Importantly, this behavior would not be captured by mass balance models that assume melting occurs only when air temperatures exceed 0°C (Huss and Hock 2015; Radić et al. 2014), indicating that such methods may indeed by unsuitable for HMA (Litt et al. 2019). However, to what extent any melt would contribute to runoff (rather than refreezing at some point before leaving the glacier) remains to be determined. The anomalously warm borehole ice temperatures observed well

above the mean annual air temperature on the lower Khumbu Glacier by Miles et al. (2018) are certainly consistent with significant latent heat release from refreezing of meltwater in the Western Cwm.

The high insolation that could enable considerable melt to occur at Camp II may also trigger melting at the South Col, with our simulation generating around 60 mm of meltwater despite a peak daily mean air temperature of –10°C (on 30 July), and not a single hourly mean air temperature above the melting point (maximum was –2.6°C on 7 July).[3] While such melt totals cannot be confirmed, we do find evidence of the surface repeatedly reaching the melting point during episodes of snow cover, when there is also generally good agreement between observed and modeled surface temperatures, despite the simplicity of our idealized snow surface (appendix C). These SEB results therefore indicate snowmelt is possible right up to the altitude of the South Col, meaning melting may be not be uncommon up to the very tops of all but a handful of the highest mountains in the Himalaya (only 14 peaks on Earth are above 8,000 m MSL). For the South Col itself, we also expect that substantially more melt occurs than indicated for the idealized snow surface, as glacier ice is exposed at the South Col. Rerunning the SEB model for such a plausible ice surface suggests melt totals of over 2 m are possible (appendix B). The substantial increase is consistent with a very strong sensitivity to albedo, which follows from the high levels of insolation.

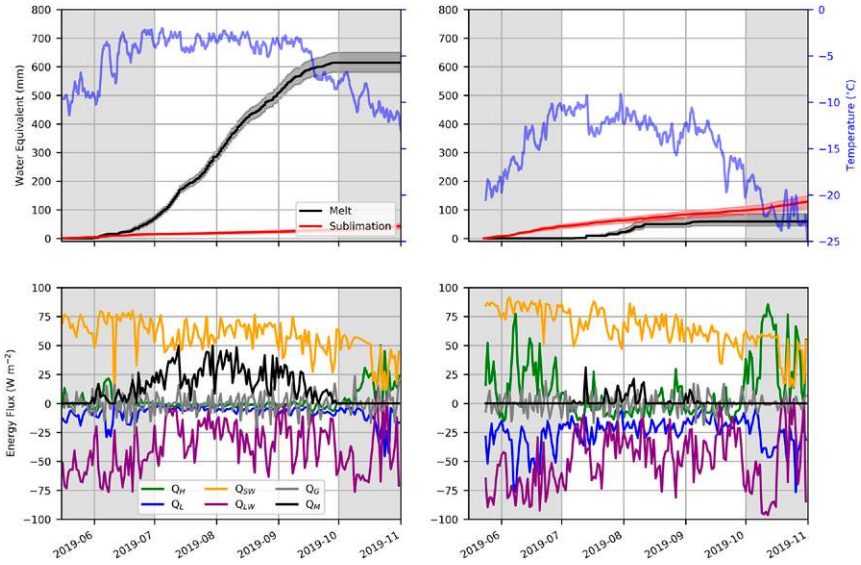

Fig. 5. Simulated mass loss and energy fluxes at (left) Camp II (6,464 m) and (right) the South Col (7,945 m). (top) Cumulative mass losses and daily mean air temperature, with shaded envelope spanning the daily minimum and maximum temperatures. The shaded envelope on the melt and sublimation curves indicates the uncertainty from perturbing the roughness length between the 5th and 95th percentiles of values reported in the literature for low-latitude snow-covered glaciers (see appendix B). (bottom) Mean daily energy fluxes, with notation consistent with Eq. (1).

Table 3. Mean and standard deviation (of daily means) for the surface energy fluxes modeled for Camp II (6,464 m) and the South Col (7,945 m). See Eq. (1) and surrounding text for details of the notation used for the respective energy components.

	Camp II (W m^{-2})		South Col (W m^{-2})	
Energy flux	Mean	Std dev	Mean	Std dev
Q_{SW}	57.6	16.2	65.2	17.4
Q_{LW}	–38.1	20.5	–49.4	24.9
Q_H	2.5	9.3	10.8	25.0
Q_L	–8.2	6.7	–25.2	13.2
Q_G	0.2	9.7	0.1	7.9
Q_M	14.0	14.3	1.4	4.4

The SEB analysis raises the question as to whether melt may even occur at the summit of Everest. We provide a first-order assessment of this by conservatively[4] extrapolating meteorological variables to 8,850 m MSL and rerunning the SEB model for the same prescribed snow surface. Uncertainties in the extrapolation are considerable (appendix D), but we *cannot* rule out that limited melting during the monsoon may be occurring at the summit (Fig. 6). We find four days on which the simulated surface

[3] We caution that the highest temperatures may be prone to positive bias if observed during strong solar heating and low wind speeds. This value occurred under winds of only 0.2 m s^{-1} and insolation of 1,161 W m^{-2}.

[4] Summit temperatures were estimated with a method designed to be robust to solar heating of temperature sensors in the AWS network (appendix D).

temperature reached the melting point under light winds and high relative humidity (generally over 80%). Under such conditions turbulent and longwave dissipation of the intense shortwave is suppressed, permitting modeled melt with air temperatures below –12°C.

Although melting at the highest point on Earth may have strong symbolic significance, sublimation seems to be a far greater means of mass loss at extreme altitude on Everest, with over 100 mm simulated for the summit and South Col (Figs. 5 and 6). The higher totals at these altitudes compared with that at Camp II (less than 50 mm) reflect the increased winds higher on the mountain that enable latent heat transfer to more efficiently dissipate the net solar radiation, which also amplifies with altitude (Table 3). The amount of mass potentially lost by sublimation on the upper slopes of Everest, coupled with the presence of permanent snow cover over much of this terrain, raises the interesting prospect that snowfall at such altitudes in the Himalaya may be more substantial than previously thought. For example, the modeled sublimation of 128 mm at the South Col (in five months) is almost 8 times greater than the predicted *annual* precipitation at such altitude (Salerno et al. 2015). Windblown snow from lower elevations may account for much of the discrepancy, but the winds are also known to deflate the snow on Everest, sometimes to spectacular effect (Moore 2004). Future work is clearly needed to rule out the possibility of a much more vigorous hydrological cycle at these extreme elevations.

Improved Everest weather forecasts. Ascending to the summit of Everest requires the relatively light winds characteristic of high pressure conditions, with climbers otherwise at much greater risk from cold injury and death (Firth et al. 2008; Moore and Semple 2011). The performance of forecasts made in support of climbing expeditions is largely unknown due to the absence of in situ observations for evaluation. We demonstrate another sample application of the new AWS data here by addressing this gap to provide the first comparison of numerical weather forecasts against actual observations from high on Everest.

During the 2019 Everest Expedition, our AWS installation team used operational deterministic forecasts from the 0.25° version of the Global Forecast System (GFS) run by the U.S. National Weather Service, and from the 0.1° HRES model run by the ECMWF. We assess the performance of these models here over the concurrent period that the AWSs have been operating, and that we have been archiving the forecasts (6 June to 31 October 2019). The forecasts are assessed for wind speed (which is often the limiting factor deciding when to climb) using data interpolated from pressure levels (for the GFS) and from model levels (for HRES) to the locations of the South Col AWS, the windiest of the locations monitored (see initial observations). Forecast skill is quantified for each forecast lead time (t) using the mean absolute error (mae):

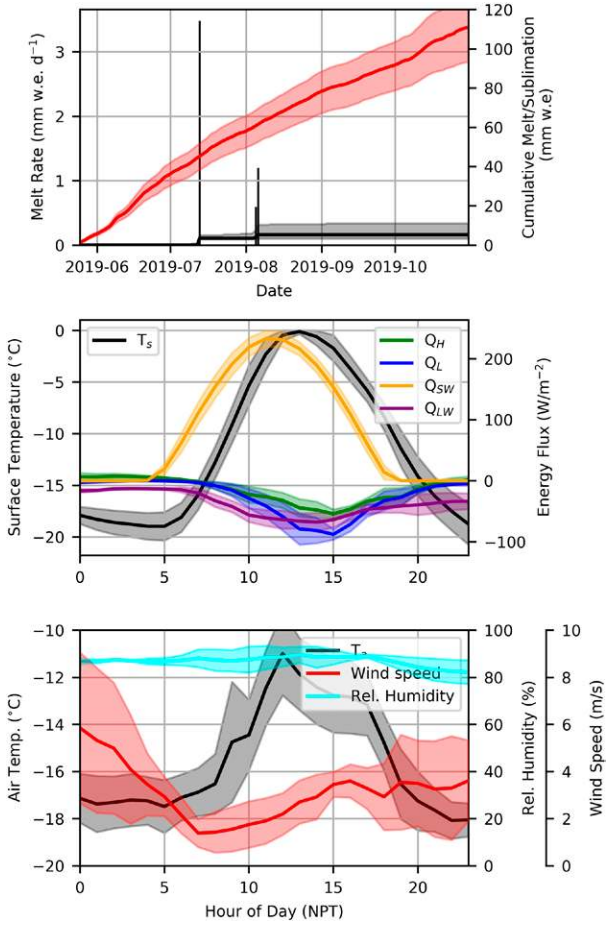

Fig. 6. Simulated mass losses, energy fluxes, and selected meteorological variables estimated for the summit. (top) Sublimation and melt, with the shaded envelope indicating the uncertainty from perturbing the roughness length (see Fig. 6 caption and appendix B). (middle) Mean plus and minus one standard deviation of energy fluxes and surface temperatures (T_s) as a function of hour of the day for all (four) days on which simulated melt for the summit was nonzero. (bottom) As in the middle panel, but for selected meteorological variables.

$$\mathrm{mae}(t)=\frac{1}{n}\sum_{i=1}^{i=n}|o_i-y_i|, \tag{2}$$

where o denotes the hourly-mean wind speeds observed at the South Col AWS, and y is the mean wind speed from the respective forecasts. Skill scores (SS) are used as a basis to compare forecasts (Wilks 2011):

$$\mathrm{SS}(t)=1-\frac{\mathrm{mae}}{\mathrm{mae}_{\mathrm{ref}}}, \tag{3}$$

where we begin by calculating $\mathrm{mae}_{\mathrm{ref}}$ from a simple forecast of persistence for different lead times:

$$\mathrm{mae}_{\mathrm{ref}}(t)=\frac{1}{n-t}\sum_{i=t+1}^{i=n}|o_{i-t}-o_i|. \tag{4}$$

With SS > 1 the results indicate that, except for 24-h HRES, both models are an improvement on the persistence forecast. They also show without exception that mae is smallest for the GFS at all lead times (Fig. 7). However, correlations between the forecast and observed wind speeds indicate strong covariation, enabling application of model output statistics (MOS) (Carter et al. 1989) through linear regression to improve the forecasts. We pursue this here using separate coefficients for each lead time, with the MOS prediction given by

$$X_{\mathrm{MOS}}(t)=\alpha_t+\beta_t X_t, \tag{5}$$

in which X_t is the raw wind speed forecast. The updated SS values (now defined with $\mathrm{mae}_{\mathrm{ref}}$ calculated on the uncorrected forecasts) indicate that applying MOS improves both models, but most notably HRES, which now outperforms the GFS at all lead times considered (Fig. 7).

To explore the skill of these MOS forecasts in more detail, we focus on hourly mean winds for a forecast lead time of 48 h. This time horizon is critical for planning the final and most dangerous climbing stage because mountaineers attempt the summit approximately this long after deciding to leave Camp II on Everest's main southern climbing route. We also highlight in Fig. 7 the performance in the premonsoon period of June (see initial observations for timing of the monsoon) because this is the

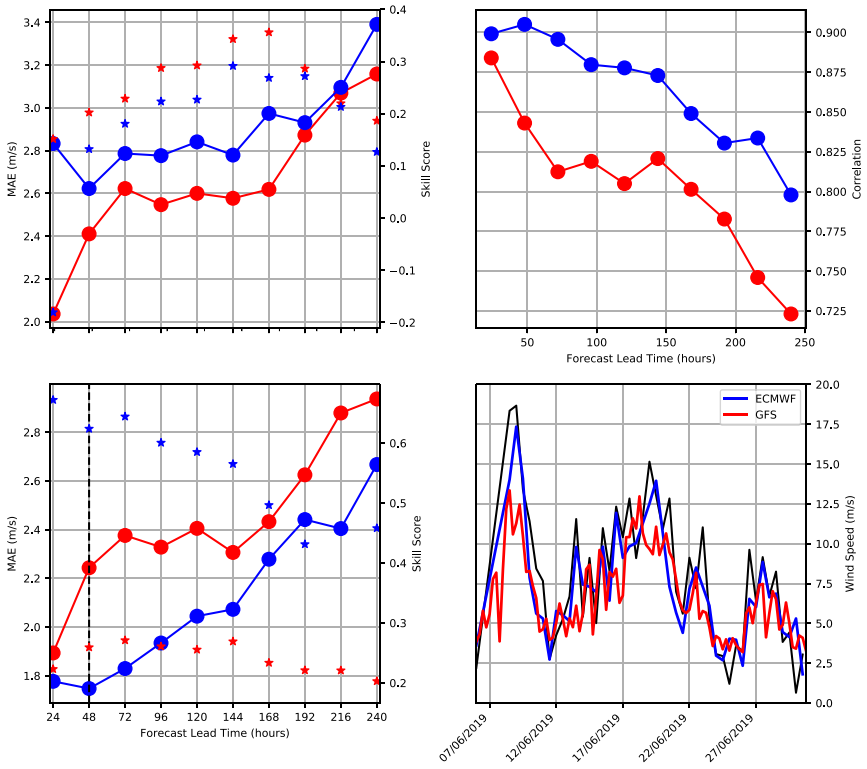

Fig. 7. Performance of the GFS and HRES wind speed forecasts at Everest's South Col (7,945 m). (top left) MAE and skill scores (SS) as a function of lead time. Note that the skill score here is computed with a simple persistence forecast as the reference. (top right) Pearson product moment correlation coefficients between observed and forecast hourly mean wind speed as a function of forecast lead time. (bottom left) As in the top-left panel, but for forecasts corrected with MOS. Here, the skill scores are computed for the MOS forecasts relative to the uncorrected forecasts. The vertical dotted line marks the performance at 48 h. (bottom right) The forecast for the 48-h lead time, during the premonsoon month of June 2019.

season when most climbing takes place (Hawley and Salisbury 2007). Both models capture the timing of enhanced winds, which peaked in early June when wind gusts were of a similar strength to those estimated for the infamous and deadly 1996 storm (Fig. 4; Moore and Semple 2006). HRES MOS also captures the magnitude of these winds well, but GFS MOS underestimates their intensity (by ~30%).

The ability of both models to correctly forecast rapid acceleration in the winds is encouraging, particularly given the somewhat modest ability noted of reanalysis data to capture the passage of extremes (Moore and Semple 2004). This improvement may be because the GFS and HRES have relatively high spatial resolutions compared with reanalyses, or because the enhanced winds in June 2019 reflected synoptic-scale strengthening, instead of localized convection as in earlier case studies (Moore and Semple 2006, 2004). More detailed analysis during the premonsoon period is required to resolve this, which we hope will be facilitated by continued data collection from the high-altitude AWSs through at least spring 2020. In any case, this preliminary assessment of forecast performance suggests considerable scope for enhancing the safety of those trying to summit Everest. As the now owner of the AWSs, the Nepalese Department of Hydrology and Meteorology will build on this potential (and the near-real-time data feed from the AWSs) to generate more accurate, publicly available forecasts and warnings for mountaineers, at altitudes where weather predictability has been limited. This, along with additional avenues for future research, are discussed below.

Synthesis and outlook

We have described the motivation, design, and installation of the highest weather station network on Earth, whose measurements hold the potential to improve understanding of Everest's weather and ongoing climate change across the full altitudinal range of glaciers in HMA. This potential of the network has been demonstrated in sample applications, providing initial insights into potential surface energy fluxes high in the accumulation area of the Khumbu Glacier and the first assessment of weather forecasts for the summit slopes of Everest. As the AWSs enter their first winter, we await the seasonal formation of the jet stream winds (Galvin 2007). We anticipate that AWS observations during jet episodes will enable improved understanding of dangerous weather events on Everest (Firth et al. 2008; Moore and Semple 2006), aeolian transport of pollutants (Bonasoni et al. 2008) and, longer-term, the response of this globally significant wind to climate warming. Such insights may be generated using multidecadal climate reconstructions to extend short records from the AWSs (Wilby et al. 2014), but longevity of the network is clearly preferable to track emerging trends. Collaborating with the Everest climbing community to maintain the high-altitude AWSs is, therefore, a high priority. At the time of writing we are working closely with Nepalese research and climbing partners to plan the first maintenance visit targeted for 2020. We are also working with colleagues from China to consolidate the records from the AWS network reported here with observations from the north side of Everest, collected by an AWS deployed at 6,475 m MSL by a Chinese team in spring 2019, whose field efforts ran concurrently to our own.

In the near term, the data collected so far already offer rich opportunities to refine the mountain weather forecasting and melt modeling applications introduced here. For example, there is scope for the network to serve as a high-profile testing ground for developing machine learning techniques to forecast hazardous weather in complex terrain (Gagne et al. 2015), and for enabling the development of transferrable empirical models that can capture mass losses high in the accumulation zones of glaciers in HMA (Litt et al. 2019). We also note that, with a recent resurgence in attempts to climb Everest in winter without supplementary oxygen (Pokhrel 2019), there is a strong incentive to forecast oxygen availability (through its relationship with air pressure) on Everest's upper slopes. Summit conditions are, on average, very

close to the tolerance limit of hypoxia, and the relatively large pressure fluctuations in winter may push conditions dangerously close to (or beyond) this threshold (Moore and Semple 2009; Moore et al. 2012; West et al. 1983).

Further work may also continue exploring processes of mass loss on Everest's summit. Our analysis has raised the prospect that the summit is *at least close to* melting during the monsoon season. Although this cannot be confirmed until direct AWS measurements of surface temperature reach the summit itself, future refinements to modeling the SEB may more tightly constrain its probability of occurrence, and how sensitive this is to climate warming. Melting at the summit of Everest—already observed or still yet to occur—could mark the crossing of a symbolic threshold in demonstrating the impacts of climate change on our planet's most extreme environments.

Acknowledgments. This research was conducted in partnership with National Geographic Society, Rolex, and Tribhuvan University, with approval from all relevant agencies of the Government of Nepal. We acknowledge Conrad Anker and Peter Athans as inspirational mountaineers who prepared the 2019 Everest expedition team and kept them safe. We also wish to thank the communities of the Khumbu Region, Xtreme Climbers Treks and Expedition P. Ltd, and Jiban Ghimire and Shangri-La Nepal Trek Pvt. Ltd, and we further recognise the extraordinary efforts of our entire Sherpa climbing team, whose physical and mental prowess at altitude made installation of the AWSs possible. The core AWS-installation team members were: Panuru Sherpa (Sirdar), Phu Tashi Sherpa, Pemba Sherpa, Urken Lendu Sherpa, Ila Nuru Sherpa, Fura Chetten Sherpa, Lakpa Gyaljen Sherpa, Pasang Sona Sherpa, Pasang Kami Sherpa, Nima Rita Sherpa, Tenzing Gyanjen Sherpa, Nawang Phinjo Sherpa, Phinjo Sherpa, and Gyaljen Dorji Sherpa. Dawa Yangzum Sherpa, Amrit Ale, Mark Fisher, Dirk Collins, and Eric Daft are also thanked for helping to ensure a successful and safe climb conducted with good humor. Heather Guy is thanked for forecasting support, Mike Hughes and Dana Greene for AWS design considerations, and the team of engineers at Campbell Scientific, Inc (Mike Hansen, Jared Campbell, Steve Gunderson, and Gary Roberts) are acknowledged for designing the AWSs. Gian Pietro Verza is thanked for his help planning installation, Patrick Wagnon and Keith Garrett for helpful advice, and the European Centre for Medium Range Weather Forecasts is gratefully acknowledged for providing access to its forecasts. We also thank G.W.K. Moore, one anonymous reviewer, and Fae Jencks at National Geographic for their help in improving the communication of our study.

Data and code availability statement. The raw hourly AWS data used in this study are available for download at www.nationalgeographic.org/projects/perpetual-planet/everest/weather-data/.

The computer code used to model the surface energy balance is available at https://github.com/climatom/Everest_BAMS.git.

Appendix A: Database of existing automatic weather stations

In the main text we present the current distribution of AWSs worldwide. To assemble this, we downloaded the positions of all the active AWSs in the Integrated Surface Database (Smith et al. 2011), and then supplemented these with all information on high-altitude AWSs presently known to the authors. The compiled station list is available for download (https://tinyurl.com/y2lgx33o).

Appendix B: Modeling the surface energy balance

Here we present the methods used to compute the SEB for a hypothetical snow surface at the elevations of the Camp II and South Col AWSs. We start from recalling that the SEB can be written:

$$0 = Q_{\mathrm{SW}} + Q_{\mathrm{LW}} + Q_H + Q_L + Q_G + Q_M, \tag{B1}$$

in which Q_{SW} is the net shortwave heat flux, Q_{LW} is the net longwave heat flux, Q_H is the sensible heat flux, Q_L is the latent heat flux, Q_G is the ground heat flux, and Q_M is the energy available for melting. All fluxes are defined as positive when directed toward the surface.

We computed Q_{SW} from

$$Q_{\mathrm{SW}} = S_i(1-\alpha), \tag{B2}$$

where S_i is the incident flux of solar radiation measured at the AWS, and α is the albedo. We set α to be 0.80—a value on the high side for old snow (Oke 2009), but close to that measured with a handheld spectrometer by the 2019 Everest field team over an (old) snow surface at Camp II (0.83).

The new longwave heat flux Q_{LW} is the difference between the incident longwave flux recorded by the AWS (L_i) and that emitted by the snow surface at temperature T_s, which has an emissivity of ε:

$$Q_{\mathrm{LW}} = L_i - \sigma\varepsilon T_s^4, \tag{B3}$$

in which σ is the Stefan–Boltzmann constant. In our model, we use $\varepsilon = 0.98$ (Tonboe et al. 2011).

The turbulent heat fluxes (Q_H and Q_L) were computed using the bulk aerodynamic method (Hock 2005):

$$Q_H = C_H \rho c_p V (T_a - T_s), \tag{B4}$$

$$Q_L = C_L \rho L_v V (q_a - q_s), \tag{B5}$$

in which C_H and C_L are the exchange coefficients for heat and moisture, respectively; ρ is air density; c_p is the specific heat capacity of the air (1,005 J kg^{-1} K^{-1}); and L_v is the latent heat of vaporization (2,501 kJ kg^{-1}); and V is the wind speed. In Eqs. (B4) and (B5) T and q denote the air temperature and specific humidity recorded at the AWS (subscript *a*) and are modeled for the surface (subscript *s*). The exchange coefficients were calculated according to

$$C_H = \frac{k^2}{\left[\ln\left(\frac{z}{z_0}\right) - \psi_M\left(\frac{z}{L}\right)\right]\left[\ln\left(\frac{z}{z_{0T}}\right) - \psi_H\left(\frac{z}{L}\right)\right]}, \tag{B6}$$

$$C_L = \frac{k^2}{\left[\ln\left(\frac{z}{z_0}\right) - \psi_M\left(\frac{z}{L}\right)\right]\left[\ln\left(\frac{z}{z_{0E}}\right) - \psi_H\left(\frac{z}{L}\right)\right]}, \tag{B7}$$

where $k = 0.4$ is the von Kármán constant, L is the Monin–Obukhov length, z is the measurement height (m), z_0 is the roughness length for momentum, z_{0T} is the roughness length for heat, and z_{0E} is the roughness length for humidity. We prescribe z_0 to be 0.0027 m and set z_{0T} and z_{0E} to be one order of magnitude smaller. This value for z_0 is equal to the mean of those reported for snow cover on low-latitude glaciers by Brock et al. (2006), and the scaling to z_{0T} and z_{0E} is consistent with that found by Stigter et al. (2018) using eddy covariance measurements at over 5,000 m MSL on Yala Glacier (also in Nepal). The roughness lengths may, however, not be appropriate

for the high-altitude snow-covered glaciers in the Himalaya. We therefore tested the sensitivity of the results by rerunning the SEB simulations with z_0 set to the 5th (0.0009 m) and 95th (0.0057 m) percentiles of the roughness lengths reported by Brock et al. (2006) for low-latitude snow-covered glaciers. All cumulative melt and sublimation totals were then presented as an envelope bounded by results from simulations run with these upper and lower roughness lengths. The stability functions Ψ for momentum, heat, and moisture (subscripts M, H, and E, respectively) were applied to extend the bulk aerodynamic approach to nonneutral boundary layers. For unstable cases, Ψ was parameterized using the expressions of Dyer (1974); those from Holtslag and De Bruin (1988) were used for stable conditions.

The Monin–Obukhov length L requires Q_H, which introduces circularity to the SEB computation. We therefore adopted an iterative technique following Munro (1990), whereby Q_H was initialized assuming a neutral boundary layer [and the Ψ_M terms are omitted from Eqs. (B6) and (B7)]; L, Ψ, and Q_H were then updated with each iteration until the change in Q_H was smaller than 1%.

Evaluation of the turbulent and longwave heat fluxes requires knowledge of T_s. We modeled this for the hypothetical snow surface by initializing $T_s = T_A$, and then evolving T_s. according to the scheme proposed by Wheler and Flowers (2011):

$$\Delta T_s = -\frac{Q_g}{\rho_s c_s h}\Delta t, \tag{B8}$$

where c_s and ρ_s are, respectively, the specific heat capacity of ice (2,097 J kg^{-1} K^{-1}) and the density in a surface layer of depth h. We used ρ_s = 530 kg m^{-3} consistent with the mean density measured in an 80-cm snow pit at Camp II during the 2019 Everest Expedition; h was set to 0.1 m (MacDougall and Flowers 2011). To prevent unrealistically low surface temperature, we follow Wheler and Flowers (2011), limiting T_s to a lower threshold of T_c (–40°C here), and tracking additional heat losses by defining cold content (C) in a passive, secondary subsurface layer:

$$C = (T_s - T_c)\rho_s c_s h. \tag{B9}$$

The ground heat flux (Q_g) (which determines the evolution of T_s) was computed from

$$-Q_g = \left(Q_{\mathrm{SW}} + Q_{\mathrm{LW}} + Q_H + Q_L\right), \tag{B10}$$

unless calculated T_s would exceed 0°C and the cold content from the passive, subsurface layer had been eliminated (i.e., C = 0), in which case Q_g = 0 and melt energy (Q_M) was computed as

$$Q_M = \max\left[\frac{\left(T_s \rho_s c_s h - C\right)}{\Delta t}, 0\right], \tag{B11}$$

where T_s is in °C. Note that after Eq. (B11) is applied, T_s is reset to 0°C and C is reduced to max($C - T_s \rho_s c_s h$, 0). We divided Q_M by the latent heat of fusion (334 kJ kg^{-1}) to convert melt energy to millimeters of water equivalent. Sublimation was derived from the latent heat flux.

To ensure numerical stability, we calculated the SEB at a time step of 120 s after having interpolated hourly AWS data to this temporal resolution. We also performed some preprocessing of the radiation measurements. First, we used calculated top-of-atmosphere insolation to set all nighttime values of S_i and S_o to zero. Second, we identified periods when

S_o exceeded S_i (~6% of observations at the South Col, ~1% at Camp II). We interpret this as resulting from snow covering the upward-facing pyranometer, so these S_i values were replaced with $S_o \times [1/\min(0.9, \alpha_{acc})]$, where α_{acc} is the "accumulated albedo," defined as the mean 24-h albedo centered on the time step of interest (Azam et al. 2014; van den Broeke et al. 2004). In the third correction step, we replaced the measured incident longwave radiation during these periods of suspected snow cover with estimates derived from the parameterization of de Kok et al. (2020), using coefficients optimized for the locations of the AWSs.

To investigate the sensitivity of the energy balance simulations to surface type, we repeated the modeling for a prescribed glacier ice surface, with an albedo of 0.4 (measured over clean ice at Base Camp with a Hukseflux NR01 pyranometer), and a near-surface density of 910 kg m^{-3} (Fig. B1). This experiment yields insight into actual melt rates at the South Col, where there is abundant exposed ice (Fig. B2),

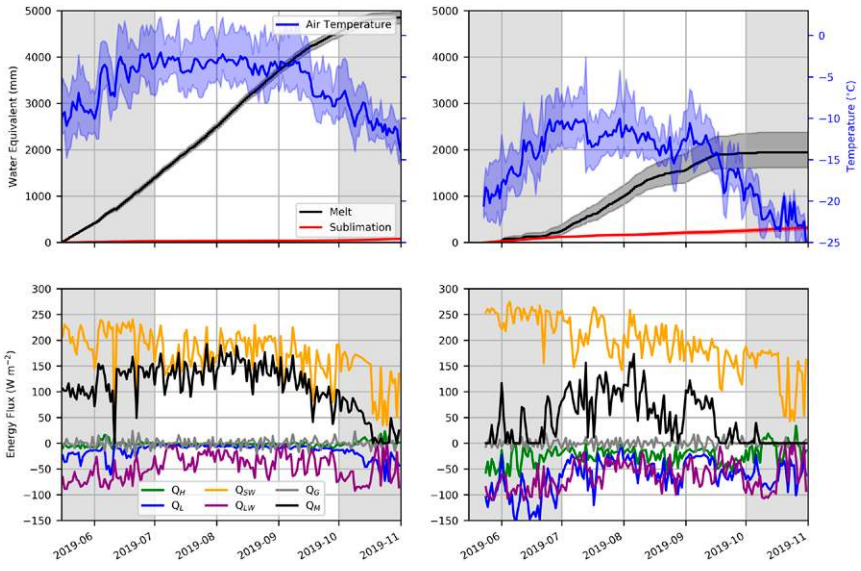

Fig. B1. As in Fig. 4, but for a hypothetical ice surface at (left) Camp II and (right) the South Col, with albedo (α) set to 0.4 and near-surface density (ρ_s) of 910 kg m^{-3}.

Appendix C: Validating melt occurrences at the South Col

We attempted to verify our conclusion that melting is possible at the South Col using the outgoing longwave flux measured at the AWS there. We made use of the fact that emitted longwave radiation (L_o) can be modeled with $\sigma\varepsilon T_s^4$ [see Eq. (B3)], and that when the surface is at the melting point T_s = 273.15 K so L_o = 309.3 W m^{-2} for ε = 0.98. However, the AWS is situated over bedrock, so to detect melt events we limited our assessment using the measured shortwave heat fluxes at the South Col to identify periods of snow with an albedo similar (±0.1) to the 0.8 prescribed in the SEB model. For this comparison, we also set z_0 to 0.0002 m (maintaining z_{0T} and z_{0E} to be one order of magnitude smaller), which is representative of fresh snow in the low latitudes (Brock et al. 2006). Examining the South Col measurements in this way suggests the following: 1) snowmelt can indeed occur at the South Col, and 2) the SEB model realistically captures its timing, with almost 70% of the melt days identified by the SEB model also detected by the observations during the period of snow cover (Fig. C1). As further support for the realism of the SEB modeling (and the conclusion that melt is possible), we note the high correlation (r = 0.93) and limited bias (particularly at the higher end of the range), in daily mean modeled and observed surface temperatures at the South Col during periods of snow cover (Fig. C2).

Fig. B2. The South Col AWS being installed. Note the tents of Camp IV in the background, and the exposed glacier ice visible behind. Photo credit: Baker Perry/National Geographic.

Appendix D: Estimating the summit weather

To assess possible mass losses through ablation and melt at the summit, we estimated the summit weather using data from the lower AWSs. For relative humidity and transmissivity (τ: the ratio of received to top-of-atmosphere insolation), summit values (Y_t) were computed at hour t from

$$Y_t = \alpha_t + \beta_t z, \qquad \text{(D1)}$$

where α and β are, respectively, the intercept and slope coefficients obtained from regressing the hourly mean meteorological quantity (Y_t) across the AWSs against their elevations (z). Note that, before applying the regression for τ, we first computed running values, defined as ratio of the 24-h sums of received, to top-of-atmosphere, insolation. We then multiplied the regression-estimated τ for the summit by the hourly top-of-atmosphere flux to estimate summit insolation.

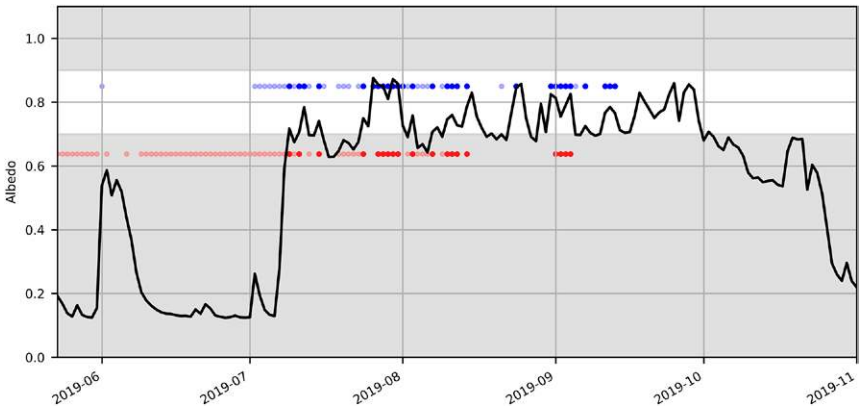

Fig. C1. Albedo and possible melt events at the South Col AWS. Blue and red dots highlight those days on which melt was modeled (blue) and observed using the outgoing longwave heat flux (red). Bold indicates days on which the albedo was between 0.7 and 0.9, identifying periods of snow cover with an albedo similar to that used by the SEB model; values outside this range are masked with gray shading.

The summit temperature was estimated with a similar linear regression technique:

$$Y_t = Y_{t,z} + \beta_t \Delta z. \qquad \text{(D2)}$$

This time, $Y_{t,z}$ is the air temperature at AWS with the highest concurrent mean hourly wind speed, and β_t is the slope of the regression line relating elevation to the 24-h running-mean air temperature at each site; Δz is the difference in elevation between the summit and the AWS with the highest mean hourly wind speed. By extrapolating air temperatures from the windiest AWS in this way, we aim to minimize positive bias in our summit air temperature estimate resulting from solar heating of temperature sensors during periods of high insolation and light winds.

The summit wind was parameterized assuming that, because the summit *cannot* be sheltered by the surrounding topography, its hourly mean speed (V_t) can be estimated as the fastest of the winds observed at either the South Col or the Balcony (the most exposed AWSs), multiplied by a scalar to account for the reduced air density at the summit (and hence greater velocity for the same driving pressure gradient; Stull 2015):

$$V_t = \max\left(V_{t,\text{South Col}}, V_{t,\text{Balcony}}\right)\frac{\rho_{t,x}}{\rho_{t,\text{summit}}}, \qquad \text{(D3)}$$

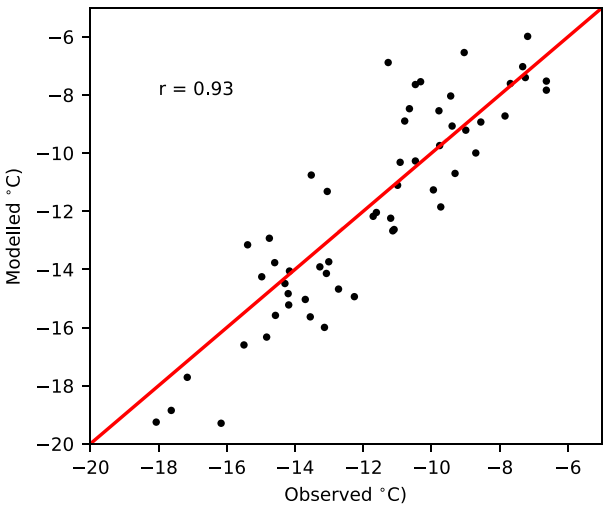

Fig. C2. Modeled and observed daily mean surface temperatures at the South Col during periods of fresh snow cover when the albedo was between 0.7 and 0.9. Note that observed surface temperature was inferred from the outgoing longwave heat flux (see text). The number annotated (*r*) indicates the (Pearson) correlation coefficient between the simulated and observed temperatures.

where $\rho_{t,x}$ is the air density at either the Balcony or the South Col, whichever has the higher hourly mean wind speed. Note that summit air density was calculated using the ideal gas law and summit air pressure, which was estimated using the hypsometric equation and the air pressure measured at Balcony:

$$P_t = P_{t,\text{Balcony}} \exp\left(\frac{8430 - 8850}{\frac{R_d}{|g|}\overline{T}_t}\right), \tag{D4}$$

where $R_d/|g|$ is the gas constant for dry air divided by the magnitude of gravitational acceleration, and $\overline{T}_t$ is the mean virtual air temperature in the atmospheric layer between the Balcony and the summit. We approximated this as the arithmetic mean of the (dry bulb) air temperature at the Balcony and (estimated) at the summit.

Finally, we parameterized incident longwave radiation using the method of de Kok et al. (2020), with coefficients optimized for the South Col (the highest AWS equipped with a longwave radiation sensor), and values of relative humidity and air temperature estimated for the summit.

Uncertainties for the inferred summit weather are shown in Table D1. They were estimated for temperature and relative humidity as 1.96 times the prediction standard deviation from the hourly elevation-based regressions (Wilks 2011); for insolation the same procedure was used to determine uncertainty in τ, before multiplying this by the concurrent top-of-atmosphere insolation. We restricted this assessment of insolation to daylight hours to avoid a low bias. Note that these uncertainties computed through regression are obtained for each hour and are summarized in Table D1 with the median.

Because longwave radiation was computed for the summit using empirical coefficients optimized for the South Col, forced with relative humidity and temperature estimated for the summit, there is opportunity for compounding errors. We neglect this complexity here and report a *lower bound* on the uncertainty, calculated as the 95th percentile in absolute differences between observed and modeled incident longwave radiation [using the method of de Kok et al. (2020)] at the South Col.

Given the different exposures of the AWSs, it is challenging to test our wind speed extrapolation between locations. We therefore do not attempt to quantify errors in summit wind speed, but caution that this source of uncertainty is likely to be large.

Table D1. Mean meteorology estimated for the Summit (8,850 m) over the period 23 May–31 Oct 2019 and associated uncertainty, summarized as the median of all hourly estimates of uncertainty.

Variable	Mean	Uncertainty
Air temperature (°C)	–20.6	2.1
Relative humidity (%)	63.7	23.0
Insolation (W m^{-2})	349.1	79.4
Incident longwave radiation (W m^{-2})	174.1	15.8

References

Abish, B., P. V. Joseph, and O. M. Johannessen, 2015: Climate change in the subtropical jetstream during 1950–2009. *Adv. Atmos. Sci.*, **32**, 140–148, https://doi.org/10.1007/s00376-014-4156-6.

Ágústsson, H., and H. Ólafsson, 2004: Mean gust factors in complex terrain. *Meteor. Z.*, **13**, 149–155, https://doi.org/10.1127/0941-2948/2004/0013-0149.

Azam, M. F., P. Wagnon, C. Vincent, A. L. Ramanathan, V. Favier, A. Mandal, and J. G. Pottakkal, 2014: Processes governing the mass balance of Chhota Shigri Glacier (western Himalaya, India) assessed by point-scale surface energy balance measurements. *Cryosphere*, **8**, 2195–2217, https://doi.org/10.5194/tc-8-2195-2014.

Bertolani, L., M. Bollasina, and G. Tartari, 2000: Recent biennial variability of meteorological features in the eastern Highland Himalayas. *Geophys. Res. Lett.*, **27**, 2185–2188, https://doi.org/10.1029/1999GL011198.

Bintanja, R., 1996: The parameterization of shortwave and longwave radiative fluxes for use in zonally averaged climate models. *J. Climate*, **9**, 439–454, https://doi.org/10.1175/1520-0442(1996)009<0439:TPOSAL>2.0.CO;2.

Bonasoni, P., and Coauthors, 2008: The ABC-Pyramid Atmospheric Research Observatory in Himalaya for aerosol, ozone and halocarbon measurements. *Sci. Total Environ.*, **391**, 252–261, https://doi.org/10.1016/j.scitotenv.2007.10.024.

Bradley, R. S., F. T. Keimig, H. F. Diaz, and D. R. Hardy, 2009: Recent changes in freezing level heights in the tropics with implications for the deglacierization of high mountain regions. *Geophys. Res. Lett.*, **36**, L17701, https://doi.org/10.1029/2009GL037712.

Brock, B. W., I. C. Willis, and M. J. Sharp, 2006: Measurement and parameterization of aerodynamic roughness length variations at Haut Glacier d'Arolla, Switzerland. *J. Glaciol.*, **52**, 281–297, https://doi.org/10.3189/172756506781828746.

Carrasco, J. F., G. Casassa, and J. Quintana, 2005: Changes of the 0°C isotherm and the equilibrium line altitude in central Chile during the last quarter of the 20th century/Changements de l'isotherme 0°C et de la ligne d'équilibre des neiges dans le Chili central durant le dernier quart du 20ème siècle. *Hydrol. Sci. J.*, **50**, 948, https://doi.org/10.1623/hysj.2005.50.6.933.

Carter, G. M., J. P. Dallavalle, and H. R. Glahn, 1989: Statistical forecasts based on the National Meteorological Center's numerical weather prediction system. *Wea. Forecasting*, **4**, 401–412, https://doi.org/10.1175/1520-0434(1989)004<0401:SFBOTN>2.0.CO;2.

Dee, D. P., and Coauthors, 2011: The ERA-Interim reanalysis: Configuration and performance of the data assimilation system. *Quart. J. Roy. Meteor. Soc.*, **137**, 553–597, https://doi.org/10.1002/qj.828.

de Kok, R. J., J. F. Steiner, M. Litt, P. Wagnon, I. Koch, M. F. Azam, and W. W. Immerzeel, 2020: Measurements, models and drivers of incoming longwave radiation in the Himalaya. *Int. J. Climatol.*, **40**, 942–956, https://doi.org/10.1002/joc.6249.

Dyer, A. J., 1974: A review of flux-profile relationships. *Bound.-Layer Meteor.*, **7**, 363–372, https://doi.org/10.1007/BF00240838.

Firth, P. G., and Coauthors, 2008: Mortality on Mount Everest, 1921-2006: Descriptive study. *BMJ*, **337**, a2654, https://doi.org/10.1136/bmj.a2654.

Gagne, D. J., II, A. McGovern, M. Coniglio, J. Correia Jr., and M. Xue, 2015: Day-ahead hail prediction integrating machine learning with storm-scale numerical weather models. *27th Conf. on IAAI*, Austin, TX, Association for the Advancement of Artificial Intelligence, 3954–3960, www.aaai.org/ocs/index.php/IAAI/IAAI15/paper/view/9724.

Galvin, J. F. P., 2007: The weather and climate of the tropics part 2—The subtropical jet streams. *Weather*, **62**, 295–299, https://doi.org/10.1002/wea.65.

Gautam, D., and S. Regmi, 2013: Recent trends in the onset and withdrawal of summer monsoon over Nepal. *ECOPERSIA*, **1**, 353–367, http://ecopersia.modares.ac.ir/article-24-11752-en.html.

Hawley, E., and R. Salisbury, 2007: *The Himalayan Database: The Expedition Archives of Elizabeth Hawley*. American Alpine Club Press, 80 pp.

Hock, R., 2005: Glacier melt: A review of processes and their modelling. *Prog. Phys. Geogr.*, **29**, 362–391, https://doi.org/10.1191/0309133305pp453ra.

Holtslag, A. M., and H. R. De Bruin, 1988: Applied modeling of the nighttime surface energy balance over land. *J. Appl. Meteor.*, **27**, 689–704, https://doi.org/10.1175/1520-0450(1988)027<0689:AMOTNS>2.0.CO;2.

Huss, M., and R. Hock, 2015: A new model for global glacier change and sea-level rise. *Front. Earth Sci.*, **3**, 54, https://doi.org/10.3389/feart.2015.00054.

Immerzeel, W. W., L. P. H. van Beek, and M. F. P. Bierkens, 2010: Climate change will affect the Asian water towers. *Science*, **328**, 1382–1385, https://doi.org/10.1126/science.1183188.

——, L. Petersen, S. Ragettli, and F. Pellicciotti, 2014: The importance of observed gradients of air temperature and precipitation for modeling runoff from a glacierized watershed in the Nepalese Himalayas. *Water Resour. Res.*, **50**, 2212–2226, https://doi.org/10.1002/2013WR014506.

——, and Coauthors, 2020: Importance and vulnerability of the world's water towers. *Nature*, **577**, 364–369, https://doi.org/10.1038/s41586-019-1822-y.

Kattel, D. B., T. Yao, K. Yang, L. Tian, G. Yang, and D. Joswiak, 2013: Temperature lapse rate in complex mountain terrain on the southern slope of the central Himalayas. *Theor. Appl. Climatol.*, **113**, 671–682, https://doi.org/10.1007/s00704-012-0816-6.

Kayastha, R. B., T. Ohata, and Y. Ageta, 1999: Application of a mass-balance model to a Himalayan glacier. *J. Glaciol.*, **45**, 559–567, https://doi.org/10.1017/S002214300000143X.

Krishnan, R., and Coauthors, 2019: Unravelling climate change in the Hindu Kush Himalaya: Rapid warming in the mountains and increasing extremes. *The Hindu Kush Himalaya Assessment: Mountains, Climate Change, Sustainability and People*, P. Wester et al., Eds., Springer International Publishing, 57–97, https://doi.org/10.1007/978-3-319-92288-1_3.

Lau, M. B., 1998: GeoPak: Monitoring climbers and climate on Mount Everest. M.S. thesis, Dept. of Electrical Engineering and Computer Science, Massachusetts Institute of Technology, 42 pp.

Litt, M., J. Shea, P. Wagnon, J. Steiner, I. Koch, E. Stigter, and W. Immerzeel, 2019: Glacier ablation and temperature indexed melt models in the Nepalese Himalaya. *Sci. Rep.*, **9**, 5264, https://doi.org/10.1038/s41598-019-41657-5.

Locci, F., M. T. Melis, F. Dessì, P. Stocchi, M. O. Akinde, V. Bønes, P. Bonasoni, and E. Vuillermoz, 2014: Implementation of a webGIS service platform for high mountain climate research: The SHARE GeoNetwork project. *Geosci. Data J.*, **1**, 140–157, https://doi.org/10.1002/gdj3.14.

MacDougall, A. H., and G. E. Flowers, 2011: Spatial and temporal transferability of a distributed energy-balance glacier melt model. *J. Climate*, **24**, 1480–1498, https://doi.org/10.1175/2010JCLI3821.1.

Meybeck, M., P. Green, and C. Vörösmarty, 2001: A new typology for mountains and other relief classes. *Mt. Res. Dev.*, **21**, 34–45, https://doi.org/10.1659/0276-4741(2001)021[0034:ANTFMA]2.0.CO;2.

Miles, K. E., B. Hubbard, D. J. Quincey, E. S. Miles, T. C. Sherpa, A. V. Rowan, and S. H. Doyle, 2018: Polythermal structure of a Himalayan debris-covered glacier revealed by borehole thermometry. *Sci. Rep.*, **8**, 16825, https://doi.org/10.1038/s41598-018-34327-5.

Moore, G. W. K., 2004: Mount Everest snow plume: A case study. *Geophys. Res. Lett.*, **31**, L22102, https://doi.org/10.1029/2004GL021046.

——, and J. L. Semple, 2004: High Himalayan meteorology: Weather at the South Col of Mount Everest. *Geophys. Res. Lett.*, **31**, L18109, https://doi.org/10.1029/2004GL020621.

——, and ——, 2006: Weather and death on Mount Everest: An analysis of the *Into Thin Air* storm. *Bull. Amer. Meteor. Soc.*, **87**, 465–480, https://doi.org/10.1175/BAMS-87-4-465.

——, and ——, 2009: The impact of global warming on Mount Everest. *High Alt. Med. Biol.*, **10**, 383–385, https://doi.org/10.1089/ham.2009.1039.

——, and ——, 2011: Freezing and frostbite on Mount Everest: New insights into wind chill and freezing times at extreme altitude. *High Alt. Med. Biol.*, **12**, 271–275, https://doi.org/10.1089/ham.2011.0008.

——, ——, P. Cristofanelli, P. Bonasoni, and P. Stocchi, 2012: Environmental conditions at the South Col of Mount Everest and their impact on hypoxia and hypothermia experienced by mountaineers. *Extreme Physiol. Med.*, **1**, 2, https://doi.org/10.1186/2046-7648-1-2.

Mountain Research Initiative EDW Working Group, 2015: Elevation-dependent warming in mountain regions of the world. *Nat. Climate Change*, **5**, 424–430, https://doi.org/10.1038/nclimate2563.

Munro, D. S., 1990: Comparison of melt energy computations and ablatometer measurements on melting ice and snow. *Arct. Alp. Res.*, **22**, 153–162, https://doi.org/10.2307/1551300.

National Geographic, 2019: Perpetual planet—Everest. Accessed 27 March 2020, www.nationalgeographic.org/projects/perpetual-planet/everest/.

Oke, T. R., 2009: *Boundary Layer Climates*. 2nd ed. Routledge, 464 pp.

Pellicciotti, F., T. Raschle, T. Huerlimann, M. Carenzo, and P. Burlando, 2011: Transmission of solar radiation through clouds on melting glaciers: A comparison of parameterizations and their impact on melt modelling. *J. Glaciol.*, **57**, 367–381, https://doi.org/10.3189/002214311796406013.

Pfeffer, W. T., and Coauthors, 2014: The Randolph Glacier inventory: A globally complete inventory of glaciers. *J. Glaciol.*, **60**, 537–552, https://doi.org/10.3189/2014JoG13J176.

Pokhrel, R., 2019: German, Spanish climbers eye toughest winter ascent on Mt Everest. *Himalayan Times*, 22 December.

Pratap, B., D. P. Dobhal, M. Mehta, and R. Bhambri, 2015: Influence of debris cover and altitude on glacier surface melting: A case study on Dokriani Glacier, central Himalaya, India. *Ann. Glaciol.*, **56**, 9–16, https://doi.org/10.3189/2015AoG70A971.

Radić, V., A. Bliss, A. C. Beedlow, R. Hock, E. Miles, and J. G. Cogley, 2014: Regional and global projections of twenty-first century glacier mass changes in response to climate scenarios from global climate models. *Climate Dyn.*, **42**, 37–58, https://doi.org/10.1007/s00382-013-1719-7.

Rounce, D. R., O. King, M. McCarthy, D. E. Shean, and F. Salerno, 2018: Quantifying debris thickness of debris-covered glaciers in the Everest region of Nepal through inversion of a subdebris melt model. *J. Geophys. Res. Earth Surf.*, **123**, 1094–1115, https://doi.org/10.1029/2017JF004395.

Salerno, F., and Coauthors, 2015: Weak precipitation, warm winters and springs impact glaciers of south slopes of Mt. Everest (central Himalaya) in the last 2 decades (1994–2013). *Cryosphere*, **9**, 1229–1247, https://doi.org/10.5194/tc-9-1229-2015.

Shea, J. M., W. W. Immerzeel, P. Wagnon, C. Vincent, and S. Bajracharya, 2015: Modelling glacier change in the Everest region, Nepal Himalaya. *Cryosphere*, **9**, 1105–1128, https://doi.org/10.5194/tc-9-1105-2015.

Smith, A., N. Lott, and R. Vose, 2011: The Integrated Surface Database: Recent developments and partnerships. *Bull. Amer. Meteor. Soc.*, **92**, 704–708, https://doi.org/10.1175/2011BAMS3015.1.

Stigter, E. E., M. Litt, J. F. Steiner, P. N. J. Bonekamp, J. M. Shea, M. F. P. Bierkens, and W. W. Immerzeel, 2018: The importance of snow sublimation on a Himalayan glacier. *Front. Earth Sci.*, **6**, 108, https://doi.org/10.3389/feart.2018.00108.

Stull, R., 2015: *Practical Meteorology: An Algebra-Based Survey of Atmospheric Science*. 1st ed. University of British Colombia, 938 pp.

Tonboe, R. T., G. Dybkjær, and J. L. Høyer, 2011: Simulations of the snow covered sea ice surface temperature and microwave effective temperature. *Tellus*, **63A**, 1028–1037, https://doi.org/10.1111/j.1600-0870.2011.00530.x.

van den Broeke, M., D. van As, C. Reijmer, and R. van de Wal, 2004: Assessing and improving the quality of unattended radiation observations in Antarctica. *J. Atmos. Oceanic Technol.*, **21**, 1417–1431, https://doi.org/10.1175/1520-0426(2004)021<1417:AAITQO>2.0.CO;2.

Viviroli, D., H. H. Dürr, B. Messerli, M. Meybeck, and R. Weingartner, 2007: Mountains of the world, water towers for humanity: Typology, mapping, and global significance. *Water Resour. Res.*, **43**, W07447, https://doi.org/10.1029/2006WR005653.

Wang, S.-Y. S., B. Fosu, R. R. Giles, and P. M. Singh, 2015: The deadly Himalayan snowstorm of October 2014: Synoptic conditions and associated trends [in "Explaining Extremes of 2014 from a Climate Perspective"]. *Bull. Amer. Meteor. Soc.*, **96** (12), S89–S94, https://doi.org/10.1175/BAMS-D-15-00113.1.

West, J. B., and Coauthors, 1983: Maximal exercise at extreme altitudes on Mount Everest. *J. Appl. Physiol.*, **55**, 688–698, https://doi.org/10.1152/jappl.1983.55.3.688.

Wheler, B. A., and G. E. Flowers, 2011: Glacier subsurface heat-flux characterizations for energy-balance modelling in the Donjek Range, southwest Yukon, Canada. *J. Glaciol.*, **57**, 121–133, https://doi.org/10.3189/002214311795306709.

Wilby, R. L., C. W. Dawson, C. Murphy, P. O'Connor, and E. Hawkins, 2014: The Statistical Downscaling Model–Decision Centric (SDSM-DC): Conceptual basis and applications. *Climate Res.*, **61**, 259–276, https://doi.org/10.3354/cr01254.

Wild, M., A. Ohmura, C. Schär, G. Müller, D. Folini, M. Schwarz, M. Z. Hakuba, and A. Sanchez-Lorenzo, 2017: The Global Energy Balance Archive (GEBA) version 2017: A database for worldwide measured surface energy fluxes. *Earth Syst. Sci. Data*, **9**, 601–613, https://doi.org/10.5194/essd-9-601-2017.

Wilkinson, F., 2019: Traffic jams are just one of the problems facing climbers on Everest. National Geographic, accessed 30 November 2019, www.nationalgeographic.com/adventure/2019/05/everest-season-deaths-controversy-crowding/.

Wilks, D. S., 2011: *Statistical Methods in the Atmospheric Sciences*. Academic Press, 704 pp.

WMO, 2019: World Meteorological Organization's World Weather and Climate Extremes Archive. Accessed 3 December 2019, https://wmo.asu.edu/content/world-meteorological-organization-global-weather-climate-extremes-archive.

Yang, X., T. Zhang, D. Qin, S. Kang, and X. Qin, 2011: Characteristics and changes in air temperature and glacier's response on the north slope of Mt. Qomolangma (Mt. Everest). *Arct. Antarct. Alp. Res.*, **43**, 147–160, https://doi.org/10.1657/1938-4246-43.1.147.

You, Q.-L., G.-Y. Ren, Y.-Q. Zhang, Y.-Y. Ren, X.-B. Sun, Y.-J. Zhan, A. B. Shrestha, and R. Krishnan, 2017: An overview of studies of observed climate change in the Hindu Kush Himalayan (HKH) region. *Adv. Climate Change Res.*, **8**, 141–147, https://doi.org/10.1016/j.accre.2017.04.001.